ENGINEERING

Bioinspired mechanical device generates plasma in water via cavitation

Xin Tang and David Staack*

Nature can generate plasma in liquids more efficiently than human-designed devices using electricity, acoustics, or light. In the animal world, snapping shrimp can induce cavitation that collapses to produce high pressures and temperatures, leading to efficient plasma formation with photon and shock wave emission via energy focusing. Here, we report a bioinspired mechanical device that mimics the plasma generation technique of the snapping shrimp. This device was manufactured using additive manufacturing based on micro–x-ray computed tomography of a snapping shrimp claw molt. A spring fixture was designed to reliably actuate the claw with appropriate force and velocity to produce a high-speed water jet that matches the cavitation number and Reynolds number of the shrimp. Light emission and shocks were imaged, which indicate that our device reproduces the shrimp's plasma generation technique and is more efficient than other plasma generation methods.

INTRODUCTION

Plasmas in and in contact with liquids are conventionally generated by intense electric fields (*1*). Such plasmas in liquids are studied from two perspectives: chemical processing and analytics, and physics fundamentals of high-energy density states and energy focusing, such as hydrodynamic cavitation luminescence (*2*–*5*), sonoluminescence (*6*–*13*), and x-ray (*14*). In engineering applications, such as fuel reforming (*15*, *16*) and water treatment (*17*), high efficiency is preferred because it affects the final processing economics. For applications in elemental detection (*18*, *19*), material processing (*20*), and medical treatments (*21*), efficiency is important because of the necessity of compact, low-cost, and controllable plasma sources.

For some species of snapping shrimp, cavitation generation is used in hunting (*22*), defense, intraspecific communication (*23*), and tunneling activities (*24*), all of which can emit light (*25*), indicating plasma generation. The shrimp's plasma generation technique may be very efficient because of evolutionary pressure (*26*–*29*). Versluis *et al.* (*30*) and Lohse *et al.* (*25*) investigated the cavitation dynamics and light emission process using a live snapping shrimp (*Alpheus heterochaelis*). Snapping shrimp generate cavitation by shooting out a high-speed water jet with a sudden snap of its large snapper claw, which makes a loud crackling noise (*31*, *32*). The compression process after cavitation initiation is so intense that gases inside the cavitation reach high temperatures capable of generating plasma and light emission (*25*, *30*). This light emission phenomenon is similar to sonoluminescence in that it occurs at the high-pressure, high-temperature singularity following the collapse of a cavitation bubble. Electrically induced microbubbles and plasmas (*33*–*35*) and laser-induced cavitation bubbles (*36*–*38*) are slightly different; they initiate as a high-pressure, high-temperature luminescent singularity, which then expands and oscillates as a cavitation bubble. Attempts to mimic the shrimp have been made; however, none have accurately reproduced the cavitation mechanism. Hess *et al.* (*39*) designed a scaled-up 70× mechanical device with the two-dimensional (2D) midplane curves of the plunger and socket. This bioinspired device was designed to match the Reynolds number of the shrimp and was able to reproduce some of the vortex formation mechanism but did not reproduce the cavitation. The corresponding computational fluid dynamics simulations were conducted on the basis of the same device by Koukouvinis *et al.* (*40*). A Ninjabot mimicking the mantis shrimp's physical musculature (*39*, *41*–*43*) was built by Cox *et al.* (*44*). This was used to investigate the mechanical principles, fluid mechanics, and cavitation; however, Cox's design generated cavitation along the whole appendage unlike the shrimp's appendage. These two independent devices highlight design aspects of sudden energy release, morphology, and nondimensional scaling; however, neither of these works used morphologically accurate shrimp claw mechanisms to study cavitation phenomena.

This paper aims to study and artificially reproduce the cavitation's generation and collapse, shock wave, and plasma generation purportedly generated by the shrimp. We designed and manufactured a scaled-up (5×) mechanical claw device using additive manufacturing with 3D surfaces based on micro–x-ray computed tomography (μ-CT) scanning of an *Alpheus formosus* shrimp claw. The bioinspired device facilitates repetitive and consistent experiments on cavitation processes and plasma generation. We anticipate to fill the aforementioned gap in previous works and accumulate authoritative evidence of mechanically generated plasma in cavitation luminescence and, in doing so, learn more about the snapping shrimp, energy focusing, and underwater plasmas. With the bioinspired idea, these fundamental understandings will enable us to design more efficient systems.

RESULTS

Design of the bioinspired device

Although previous research done by Hess *et al.* (*39*) used only the 2D midplane curve of the snapper claw, they did successfully obtain 3D claw morphology information for a single species of shrimp, *Alpheus bellulus*. The species of shrimp used in this project is *A. formosus* (Fig. 1A) (*45*), which were purchased from the eBay seller "peppermint-shrimp" and kept in a saltwater aquarium for months while snapper claw molts were collected for the project.

A snapper claw molt (Fig. 1B) was collected for μ-CT scanning and, via surface determination, was converted into a mesh file that contains claw morphology information and quantitative 3D geometrical

Department of Mechanical Engineering, Texas A&M University, College Station, TX 77843, USA.
*Corresponding author. Email: dstaack@tamu.edu.

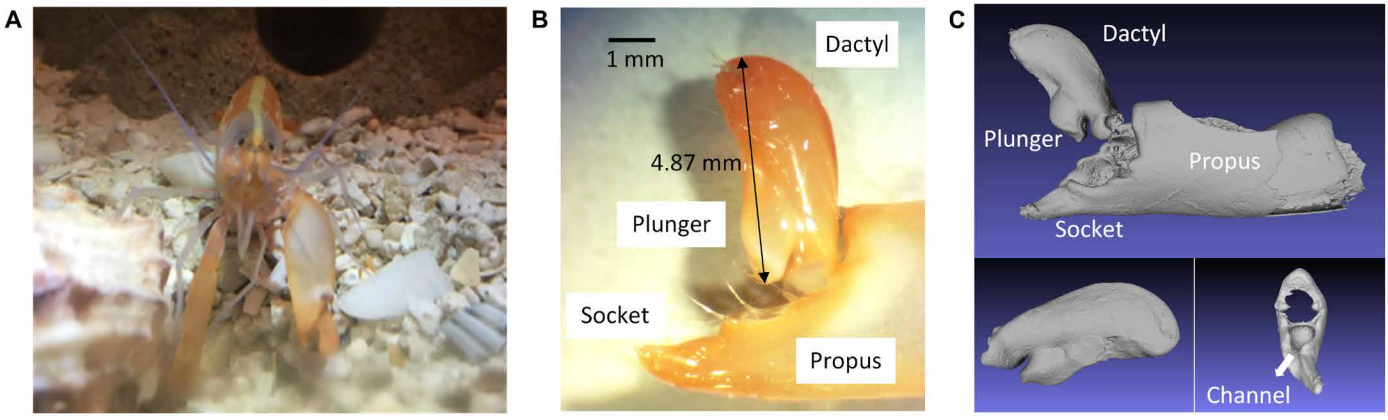

Fig. 1. Snapper claw morphology of the snapping shrimp *A. formosus*. (**A**) *A. formosus*, the striped snapping shrimp. Photo credit: David Staack, Texas A&M University. (**B**) Microscope image of the snapper claw molt. The claw consists of plunger, dactyl, socket, and propus. Photo credit: Xin Tang, Texas A&M University. (**C**) 3D rendering of converted snapper claw mesh shown in MeshLab. There is a water channel at the exit of the socket, forming a nozzle throat with rotating dactyl and plunger during the claw closing process.

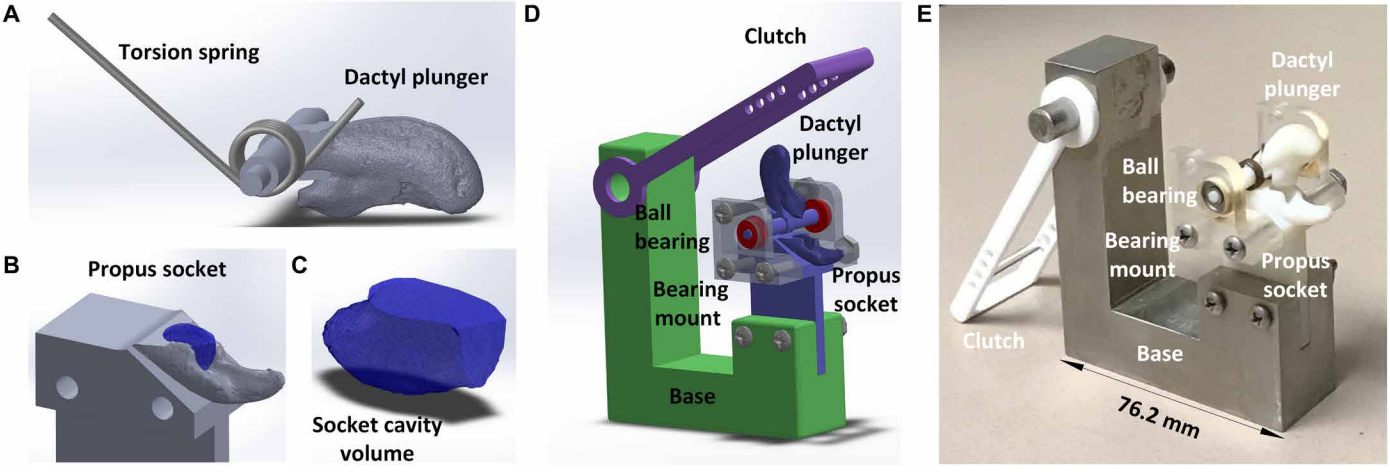

Fig. 2. CAD model. (**A**) Dactyl plunger with step shaft and torsion spring. (**B**) Immobile propus and socket cavity volume, with a socket exit channel width of 3.3 mm. (**C**) Socket volume geometry captured in CAD. (**D**) CAD model of the bioinspired device. (**E**) Manufactured bioinspired device with torsion springs. Photo credit: Xin Tang, Texas A&M University.

data of the snapper claw. With careful modifications such as bridging and filling cavity holes in the model and reducing unnecessary points and surfaces in MeshLab (*46*, *47*), the open claw was divided into two separate manifold parts: the dactyl part and the propus part (shown in Fig. 1C, bottom left and right, respectively).

After refining morphology data from the snapper claw and importing the solid body file into SolidWorks, the two claw halves were aligned by assigning an axis of rotation that would ensure proper clearance. Minor material wear during operation further ensured a proper fit. Torsion springs were used to mimic the torque applied by the shrimp's muscle. The claw's dactyl had the largest dimension of 4.87 mm but was fabricated at five times the actual size to facilitate manufacture and mechanical integration. An ordinary differential equation (ODE) numerical model characterized the dactyl dynamics with simplified physical aspects (see details in text S1 and fig. S1) and was implemented to improve the design and match nondimensional Reynolds and cavitation numbers and other parameter selection.

The snapper claw mechanism consists of two major components that contribute to proper operation: the plunger and the socket (labeled in Fig. 1C). The plunger tightly fits into the socket, which displaces all the water inside the socket through the nozzle-shaped channel. The rapid acceleration of the dactyl induces the high-speed water jet to issue from the channel and initiate cavitation. An angle of approximately 25° exists between the water channel direction and rotation plane of the plunger. This angle may exist evolutionarily to enhance cavitation in a targeted direction and physically separate the cavitation from the dactyl surface, which results in an isolated cavitation collapse without self-inflicted cavitation damage (movie S1). The back of the dactyl was modified for attachment of the torsion spring and flanged ball bearing assembly (Fig. 2A), while the propus was mounted rigidly below the dactyl (Fig. 2B). The final cavity volume is approximately 222.89 mm^3 (Fig. 2C). We believe that all the elements described above are essential to the claw morphology and process, and need to be inherited in the bioinspired design.

An additive manufacturing process (commonly known as 3D printing) was used to fabricate the complex geometry of the bioinspired claw. Major 3D-printed parts ordered from Shapeways were the dactyl and propus, together with the clutch. These parts were

printed using "white strong flexible plastic" (EOS PA2200) because of its strength and low moment of inertia. Although accidental snapping of the claw in air will destroy it, this does not happen in water because of the increased drag. A rendering of the claw's CAD (computer-aided design) model along with a photo of the final bioinspired device can be seen in Fig. 2 (D and E).

High–frame rate videography

High–frame rate videography of the bioinspired device in operation underwater was taken using a charge-coupled device (CCD) camera (Photron, FASTCAM SA5), which is capable of 1 million frames per second (fps). This camera was used to estimate dactyl tip speed and to image cavitation evolution at a frame rate of 60,000 fps. A series of selected high–frame rate video imaging stills of the rotating dactyl driven by two weak torsion springs with front lighting are shown in Fig. 3A to illustrate claw operation (stills from movie S2). Two major cavitation sites were spotted: one from the water jet and the second along the tip of the claw. This leads to one implosion singularity site at the surface of the dactyl and another one located at a distance from the dactyl, generated by the high-speed jet. The cavitation generated by the high-speed jet is spheroid-like and oscillatory in time (Fig. 3A). Because the cavitation volume was difficult to estimate accurately, an effective radius (Fig. 3B) was approximated by assuming a volumetric equivalent ellipsoidal cavitation with major and minor axes measured from the video.

The dactyl dynamics ODE model was used to make comparison to experimental video data obtained via feature tracking. Figure 3C highlights this comparison. According to experimental data, the maximum speed of the dactyl tip was 20.9 ± 2.6 m/s, the duration of sweep was approximately 1.5 ms, and the stopping time was 1.2 ms. The cavitation front propagation speed can be used as a close estimation for water jet speed, shown in Fig. 3D. With a maximum cavitation front speed of 25.6 to 37.4 m/s, this implies Reynolds numbers of 0.84×10^5 to 1.23×10^5 and a cavitation number of $\sigma = 0.14$ to 0.30, which are comparable to the real shrimp (for details, see text S1) (*30*).

Schlieren imaging of shock wave underwater

Snapping shrimps contribute to underwater noise throughout the world's tropical and subtropical shallow ocean waters (*48*), because shock waves are generated during the snaps of their snapper claws (*30*). Schlieren imaging can be used to uncover details of shrimp-produced shock wave generation and propagation.

The schlieren setup in this project uses the popular Z-type two-mirror Herschellian schlieren configuration (see fig. S2A) (*49*). Multi-exposure images of the propagating shock wave generated by the bioinspired device and corresponding hydrophone and intensified CCD (ICCD) shutter signals are exhibited in Fig. 3 (E and F). In Fig. 3E, the three exposures show the expanding shock front generated by the first singularity of collapsing cavitation. The cavity and site of singularity is spotted at the center of the spherical shock wave and offset from the tip of the claw. This visualization shows that the shock (used by shrimp to stun prey) comes from the collapsing cavitation, as proved previously (*30*). The shock wave front speed was determined to be 1487.9 ± 39.7 m/s, the sound speed of water (fig. S2, B to D, and table S2).

Light emission detection for saline water with air doping

Light emission from collapsing cavitation produced by the bioinspired device is very dim, hardly observable by the naked eye in a darkroom. The duration of such light emission could occur at nanosecond (*25*) time scales, which is similar to a single sonoluminescence event (*8*). Initial attempts to measure light emission from the device

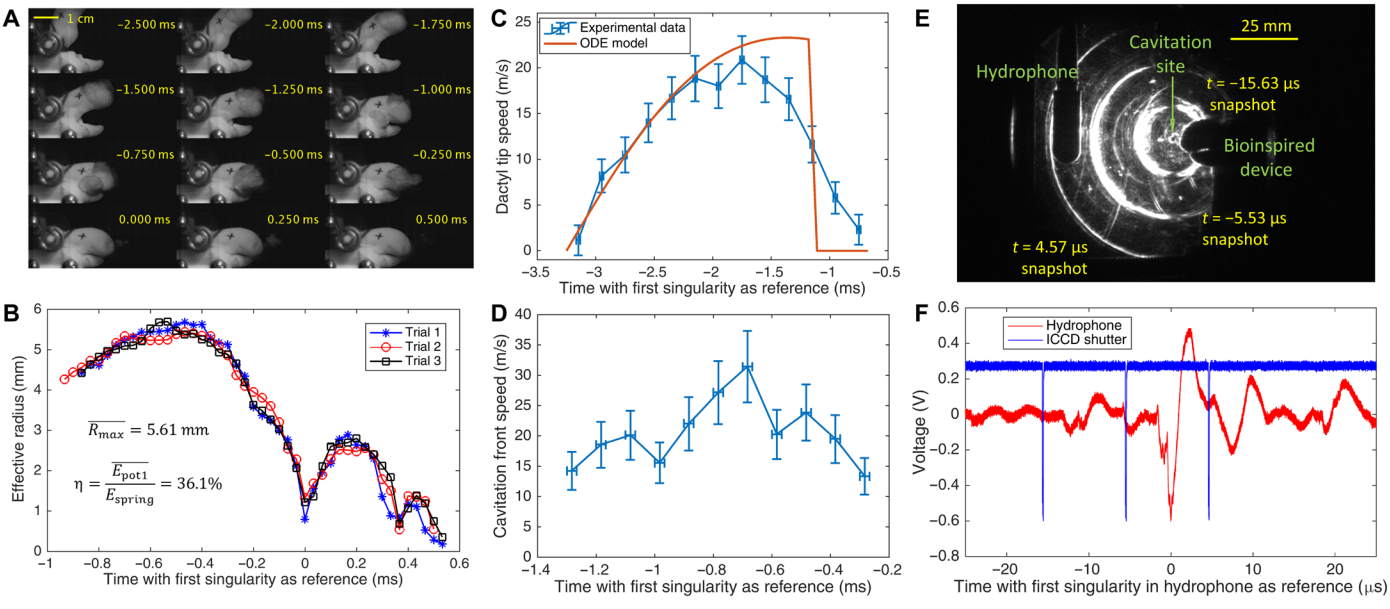

Fig. 3. High–frame rate video images and schlieren images with double weak torsion spring configuration. (**A**) Selected high–frame rate video frames during device operation, emphasizing cavitation evolution. The raw video was recorded at 60,000 fps (movie S2), with $t = 0.000$ ms corresponding to the first singularity, when the first minimum was reached by the collapsing cavitation. (**B**) Plot of effective radius over time for three different trials, with an average maximum radius of 5.61 mm and an average conversion efficiency of 36.1% (see text S3). (**C**) Comparison of device dactyl tip speed experimental data with the numerical model result. (**D**) Cavitation front speed estimation due to the high-speed water jet. (**E**) Superposition of three schlieren images during device operation showing shock wave propagation, with 100-ns exposures and 10 μs of delay between images. (**F**) Hydrophone (red) and ICCD shutter (blue) signals during the first singularity, which occurred at around $t = -25$ μs.

in distilled water using an ICCD camera did not yield conclusive results; to solve this issue, argon doping (*50*) and air doping were introduced to promote light emission.

To verify the consistency of the bioinspired device and identify the region of interest, we took several 1360 pixel–by–1024 pixel 12-bit images of the bioinspired device during operation in distilled water using an ICCD camera with a hydrophone trigger located 5 cm away from the cavitation region at various delay times (Fig. 4A). The major cavitation singularity site location appeared to vary by ±3 mm from snap to snap. The hydrophone signal that triggered the camera was caused by sound from the manual clutch release and was therefore prone to jitter. To address this jitter, we used a relatively long exposure time of 20 μs to image the first singularity.

Saline water [35,000 ppm (parts per million) NaCl] was used to simulate the snapping shrimp's living condition in the ocean. To determine the time scale of the light emission process, we set up a photomultiplier tube (PMT) on the opposite side of the water tank to measure nanosecond time scale light emission in parallel with the ICCD camera (fig. S3). To reduce background noise, we turned off or blocked all light sources in the laboratory dark room. Twenty hydrophone-triggered images were taken, and then the location of all pixels with an intensity significantly above background was cataloged (see Materials and Methods); a probability distribution histogram of average above-threshold pixel intensities is shown in Fig. 4B. The location of these above-threshold pixels (corresponding to cavitation luminescence sites) is presented in Fig. 4C, superimposed on a reference image to show the consistency of the first singularity position. The chosen detection threshold is nine SDs above the average of background noise; therefore, any signal above this can be confidently interpreted as light emission. While light has been detected before from a shrimp or shrimp-like cavitation system (*25*), this is the first imaging of the light emission and directly correlates the light with the cavitation singularity site.

Unlike the ICCD, the PMT can measure nanosecond time scale changes in light emission for a narrow region of interest. The ICCD images and corresponding PMT signals of claw-induced light emission in saline water with air doping are presented in Fig. 5. A large localized cavitation and light emission event can be spotted in the ICCD image (Fig. 5A), with a spatial diameter around 118.3 μm. While the cavitation oscillated, two substantial short [≤13-ns full width at half maximum (FWHM)] light pulses were observed in the PMT signal (Fig. 5B), which prove that there was light emission from the first and second cavitation singularities.

According to data from trial #15 (Fig. 5, C and D), the brightest light pulse was slightly dimmer, with light emission duration FWHM less than 14 ns. Trial #20 presented here (Fig. 5, E and F) has an above-average brightness when compared to all trials. The estimated length scale of the combined light emission area in this trial approached ~600 μm and had a slightly longer duration (less than 17 ns for FWHM), which can be attributed to the contribution of several small light emission events occurring in quick succession. The comparison of PMT signal and ICCD image intensity is shown in text S4. Some discrepancy is caused by the difference in the region of interest of both devices, lens attenuation difference, and quantum efficiency difference. On the basis of all results from this experiment, an interesting trend emerged, which suggests that a single coherent cavitation site may enhance the light emission phenomenon and improve energy focusing compared to a cavitation

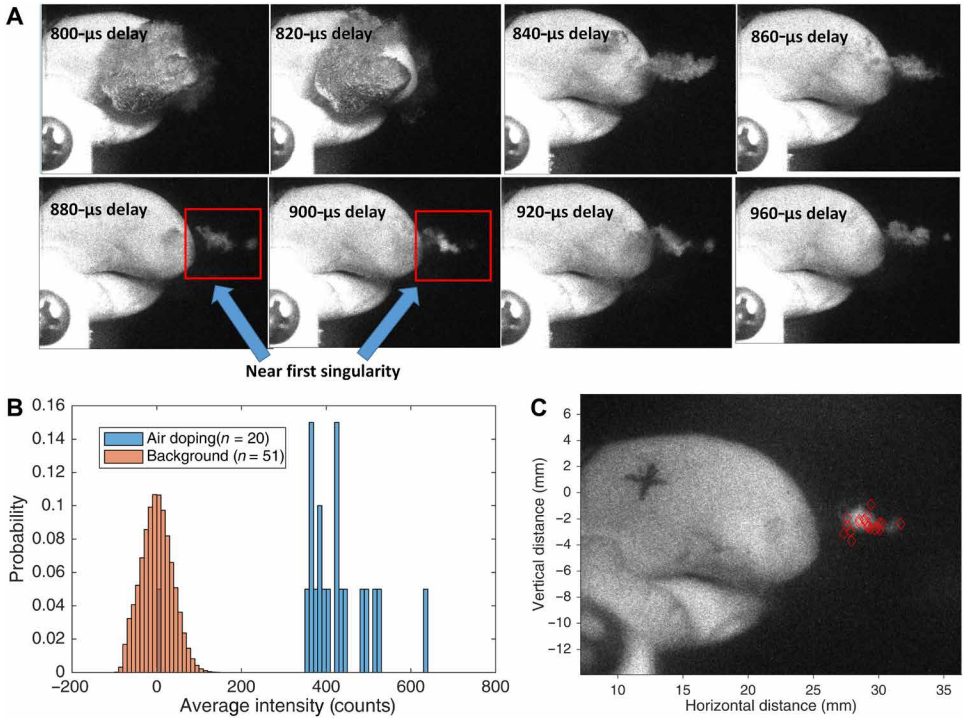

Fig. 4. Light emission imaging and brightness statistics for the bioinspired device operating in saline water. (**A**) Shrimp claw imaging at different delay times using 20-μs ICCD exposure, highlighting the delays that correspond to cavitation singularities. (**B**) Probability distribution of the average intensity (in ICCD counts) of pixels above threshold for different trials using saline water with air doping (bin width, 10 counts) as compared to background signal distributions. AU, arbitrary units. (**C**) Cavitation locations (marked with red diamonds) relative to claw, as measured by ICCD.

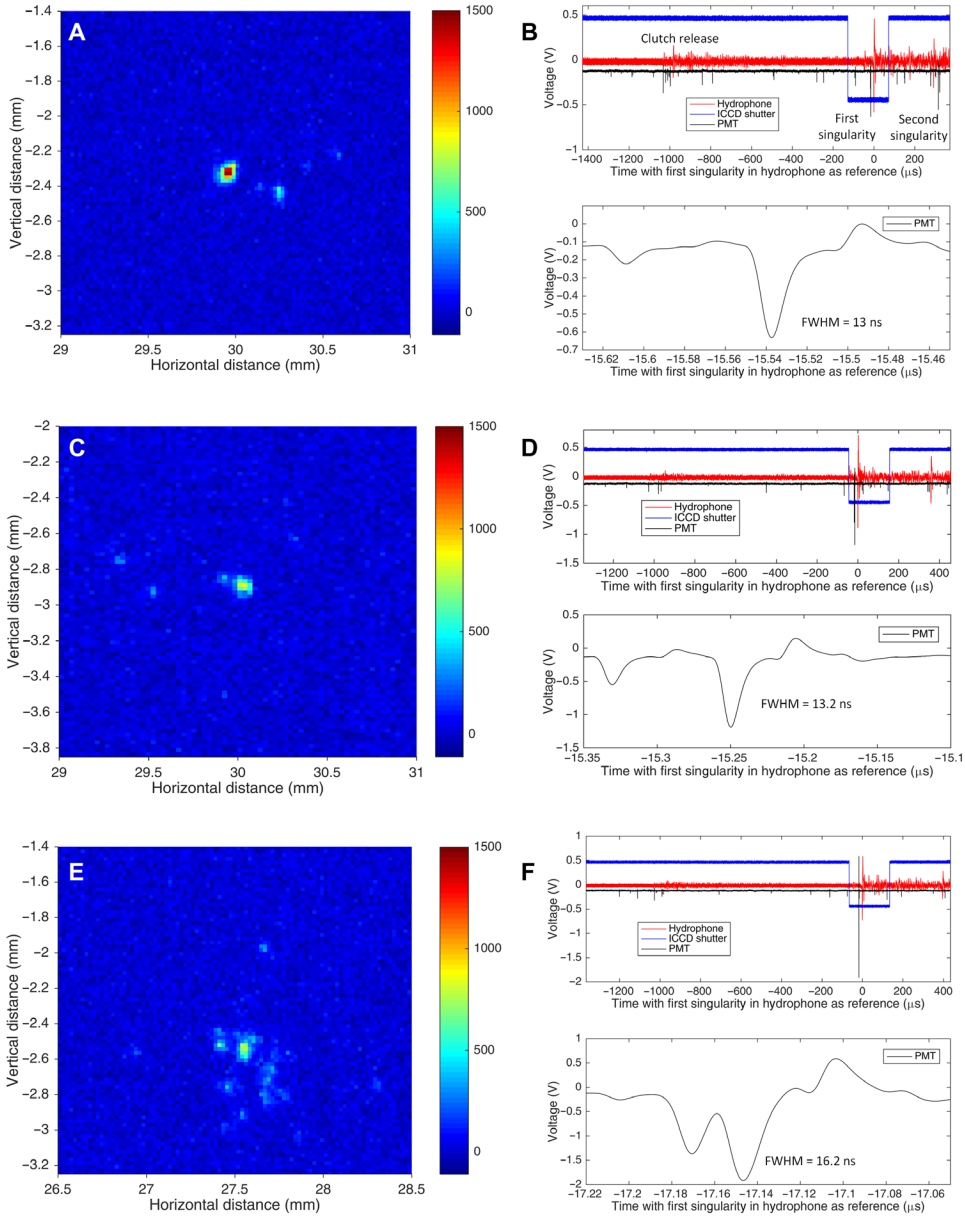

Fig. 5. Light emission in ICCD images (200μs exposure time) and corresponding hydrophone, camera shutter, and PMT signal for saline water with air doping. (**A**) Trial #4 ICCD image. (**B**) Trial #4 oscilloscope data and PMT signal zoom-in. The duration time of light emission FWHM is less than 13.0 ns. The ICCD shutter signal and PMT signal are scaled to $^1/_5$ and 5 times, respectively, for better data visualization. (**C**) Trial #15 ICCD image. (**D**) Trial #15 oscilloscope data and PMT signal zoom-in. The duration time of light emission FWHM is less than 13.2 ns. (**E**) Trial #20 ICCD image. (**F**) Trial #20 oscilloscope data and PMT signal zoom-in. The two durations of light emission FWHM are less than 16.2 ns.

cloud of numerous smaller cavitation sites. Similar results and trends were also observed using distilled water with argon doping (fig. S4) and distilled water with air doping (fig. S5). Light emissions in three cases—(i) argon in distilled water, (ii) air in distilled water, and (iii) air in saline case—were observed.

DISCUSSION

This type of bioinspired device with complex 3D surfaces, which can mimic snapping shrimp cavitation phenomena, has not been reported before. Using this device, cavitation experiments can be carried out in various fluids other than saline water, such as distilled water, mineral oil, and other fluids, in which experiments with a live marine animal is not possible. Also, this device generates well-timed repetitive cavitation events, facilitating current and future experimental design. The morphologically accurate snapper claw geometry and the dynamics of the dactyl plunger are essential for the bioinspired design of the device. The streamlined geometry plays an important role in targeting the high-speed jet out the angled channel and off the claw surface, which induces stand-alone large cavitation and avoids self-inflicted damage to the device (or shrimp). The matching of nondimensional numbers further ensures the occurrence of

the cavitation event in this scaled-up design, which is five times larger than the scanned shrimp. A factor of five scaling is still within the range of intraspecific size variation and alpheid shrimp diversity (*45*). A distilled design with the right physical mechanism can also work for different applications in the future.

The ICCD images provided strong evidence of light emission generated by the collapsing cavitation in water with either air or argon doping. Light emission indicated three modes in the device cavitation luminescence: weak emissions buried in background, which are below threshold; emissions enhanced by larger and more coherent cavitation corresponding to higher intensities; and emissions with the intermediate intensity range, where most trials located. The larger coherent cavitation generates stronger light emission signal. This variation is stochastic likely because of small initial condition variation and turbulence. Similar to what is observed with sonoluminescence, our light emission results indicate the presence of an inertially confined plasma generated by the imploding cavitation (*13*, *51*).

The bioinspired claw's efficiency, η, in converting torsion spring energy to cavitation potential energy is around 36.1%. This is based on the initial spring energy and the available energy in displacing the ambient water from the low-pressure cavity, calculated from the maximum effective radius of cavitation during operation. Applying the same calculation methods, this conversion process is more efficient than that of single-bubble sonoluminescence ($\eta_{SBSL} \approx 0.014\%$), electrically induced cavitation ($\eta_{electric} \leq 0.058\%$), and laser-induced cavitation ($\eta_{laser} < 5.8\%$) (see details in text S3). This efficiency is not luminescent efficiency, which is also affected by bubble size and shape symmetry (*52*, *53*). Temperatures, which can be estimated by the light emission spectrum inside the cavitation, are the best parameters to determine thermodynamic efficiency of the compression process for this cavitation luminescence event. Future spectroscopic study of this mechanically generated plasma phenomenon might reveal additional insights under the extreme cavitation singularity conditions.

CONCLUSION

We have constructed a bioinspired artificial mechanism that produces the same type of shock waves and plasma as that created by the snapping shrimp. Fabrication of this morphologically complicated device was made feasible by additive manufacturing. Effective cavitation occurs because of a high-velocity, well-aimed water jet. This hydrodynamic cavitation collapses to a high pressure and temperature plasma state that emits lights and shock waves upon rebounding. The physical size of the light emission area captured by the ICCD ranged from 10 to 100 μm and often occurred at multiple singularity sites, with duration FWHM of 8 to 24 ns (15 ns in average). There are several other verified methods to produce underwater plasma and achieve cavitation luminescence, such as submerged electrical breakdown, sonoluminescence, submerged laser-induced breakdown, and other mechanical devices that can produce cavitation such as Venturi tubes, hydrofoils, water hammer devices, and other biomimetic devices. Our device, inspired by the snapping shrimp's snapper claw (which has benefitted from eons of natural evolutionary improvement), create free-standing cavitation bubbles that are more efficient than those generated by the aforementioned alternate methods. Operation of our device underwater also provides insight into how snapping shrimp species create the loud snapping sound and light emission. This design can be applied to enhance microfluidics, chemical processing, physical processing, and hydroacoustics. The device can also be used in other dense fluids, as long as the fluid is compatible with materials available in manufacturing.

MATERIALS AND METHODS

3D scanning of snapper claw

The molt of the snapper claw was collected by μ-CT scanning in the Cardiovascular Pathology Laboratory at the Texas A&M College of Veterinary Medicine. The snapper claw molt was stabilized with cotton wool and scanned twice in the μ-CT (X-Tek Hawk CT and X-ray Imaging System). The first μ-CT scan imaged the claw in the open position with a resolution of 17.5 μm, and the second scan imaged the claw in the closed position with a higher resolution of 9.7 μm. The resulting 3D surface data were captured using Inspect-X and reconstructed using CT Pro. Then, the reconstructed model was converted into a mesh file using VGSTUDIO MAX 3.0, with manual adjustment of the opacity curve and thresholds for different materials, to perform surface determination. After simplifying and modifying the mesh file using MeshLab, the final product was then imported into SolidWorks for future design.

Schlieren imaging of underwater shock wave

The experimental setup used was the popular Z-type two-mirror Herschellian schlieren configuration. The illumination source was a continuous diode-pumped solid-state class IIIb laser (300 mW; Changchun New Industries Optoelectronics Tech. Co. Ltd., China), emitting light with a wavelength of 532 nm. The laser beam was then expanded to a larger-diameter collimated beam using a plano-convex lens, a plano-concave lens, and a parabolic mirror. After propagating across the image plane (water tank with bioinspired device), the collimated laser light was then reflected and focused by a second parabolic mirror and cut off by a vertical knife-edge coated with black paint. This vertical cutoff enabled observation of any horizontal gradient in refractive index in the test section. A plate with a 6.35 mm hole was placed immediately before the knife-edge to block any stray light. A single convex lens was placed after the knife-edge cutoff to increase magnification for the ICCD camera. A 4 Picos ICCD camera (Stanford Computer Optics Inc.) was used in multi-exposure mode to capture the schlieren photograph of shock wave propagation, and underwater pressure signals were monitored with a Teledyne RESON hydrophone (TC4013; 170 kHz). A multi-exposure mode was used such that multiple images from a single snap could be recorded on the ICCD before readout, which results in image data at both high resolution and high frame rate. In this case, several 100-ns exposures were delayed by 10 or 15 μs. An oscilloscope (WaveRunner 204MXi 2 GHz, 10 GS/s; produced by Teledyne LeCroy Company) was used to monitor the hydrophone signal and trigger the ICCD camera. The ICCD camera's gated exposure signal was also monitored on the oscilloscope such that relative delay between trigger and exposure could be observed.

Saline water with air doping

The saline water (NaCl solution) was prepared by mixing freshly opened distilled water and pure sodium chloride (>99%). The saline water concentration is around 35,000 ppm, which is close to the salinity of seawater where snapping shrimp live. Before carrying out light emission detection experiments, compressed air was doped

into the saline water via a bubbling disc for 30 min to ensure that the solubility of air in the water tank was saturated.

Distilled water with argon or air doping

Because no light emission was observed in distilled water tank without gas doping, argon or air was doped into the freshly opened distilled water via a bubbling disc for 30 min to ensure that the solubility of argon in the water tank was saturated. Argon was chosen initially because of its accessibility, known excitation emission spectra in the visible light range, a larger polytropic exponent at bubble collapse, and effective use in single-bubble sonoluminescence experiments.

ICCD light emission image collection and processing

The aforementioned ICCD was also used to image the light emission from the cavitation singularity using a macro lens (AF-S VR Micro NIKKOR 105mm f/2.8G IF-ED) at a 1:1 magnification ratio and f/2.8 aperture. The ICCD image exposure time was 100 or 200 μs with a gain setting of 1000 and was artificially delayed from the clutch release time sensed by the hydrophone for around 880 μs (chosen on the basis of analysis of the high–frame rate videos). This timing correlated to be around the first singularity and was long enough to account for most jitter in the clutch release and short enough to avoid excessive background signal. Multiple background images were taken without triggering the bioinspired device in a dark room. These background images were averaged and subtracted from images acquired during device operation for presentation in this article. The average intensity of background images taken for background subtraction is around 60 counts (out of 4095 counts for a 12-bit system) for distilled water and 73 counts for saline water with an average SD ($\sigma_{background}$) close to 34 ± 3 counts. For the ICCD results and images presented in this article the units are ICCD counts with average background value subtracted. For colorized ICCD images the counts values was scales to range from $3\sigma_{background}$ to maximum intensity with a jet color map to highlight light emission of interest in the image.

For analysis of the light emission ICCD images, a threshold was chosen for distinguishing background and pixels that captured the light emission. A threshold of $9\sigma_{background}$ was chosen; thus, the bright pixels above threshold were statistically significant and corresponded to light emission signals. Because of the stochastic influences in the cavitation formation and collapse, not all singularities had the same brightness. One of the 20 trials did not have light emission exceeding the $9\sigma_{background}$ threshold (see Fig. 4B). In addition, cosmic rays and similar induced excitations could randomly induce ICCD camera signal over limited pixel regions. However, such observed signals did not correlate with the expected location of the singularity or the timing from the clutch release, as was the case for light emission during the cavitation collapse, which is shown in Fig. 4C.

SUPPLEMENTARY MATERIALS

Supplementary material for this article is available at http://advances.sciencemag.org/cgi/content/full/5/3/eaau7765/DC1

Supplementary Text

Fig. S1. Rotating dactyl plunger numerical model.

Fig. S2. Schlieren imaging of underwater shock wave.

Fig. S3. Experiment setup of light emission detection with ICCD and PMT.

Fig. S4. Light emission imaging and brightness statistics for the device operating in distilled water with argon doping at 100-μs exposure time.

Fig. S5. Light emission imaging and brightness statistics for the device operating in distilled water with air doping at 100-μs exposure time.

Fig. S6. Relation between PMT signal peaks and ICCD image sum of pixel intensities above threshold (9σ).

Table S1. Measured results of underwater shock wave propagation speed.

Table S2. Torsion spring parameters.

Movie S1. High–frame rate video of the bioinspired device operation from upper view.

Movie S2. High–frame rate video of the bioinspired device operation from side view.

References (*54*–*63*)

REFERENCES AND NOTES

1. S. Samukawa, M. Hori, S. Rauf, K. Tachibana, P. Bruggeman, G. Kroesen, J. C. Whitehead, A. B. Murphy, A. F. Gutsol, S. Starikovskaia, U. Kortshagen, J.-P. Boeuf, T. J. Sommerer, M. J. Kushner, U. Czarnetzki, N. Mason, The 2012 Plasma Roadmap. *J. Phys. D. Appl. Phys.* **45**, 253001 (2012).
2. K. R. Weninger, C. G. Camara, S. J. Putterman, Energy focusing in a converging fluid flow: Implications for sonoluminescence. *Phys. Rev. Lett.* **83**, 2081–2084 (1999).
3. T. G. Leighton, M. Farhat, J. E. Field, F. Avellan, Cavitation luminescence from flow over a hydrofoil in a cavitation tunnel. *J. Fluid Mech.* **480**, 43–60 (2003).
4. M. Farhat, A. Chakravarty, J. E. Field, in *Proceedings of the Royal Society of London A: Mathematical, Physical and Engineering Sciences* (The Royal Society, 2010), p. rspa20100134.
5. C.-K. Su, C. Camara, B. Kappus, S. J. Putterman, Cavitation luminescence in a water hammer: Upscaling sonoluminescence. *Phys. Fluids* **15**, 1457–1461 (2003).
6. D. F. Gaitan, thesis, University of Mississippi (1990).
7. K. S. Suslick, Sonochemistry. *Science* **247**, 1439–1445 (1990).
8. B. P. Barber, S. J. Putterman, Observation of synchronous picosecond sonoluminescence. *Nature* **352**, 318–320 (1991).
9. W. B. McNamara III, Y. T. Didenko, K. S. Suslick, Sonoluminescence temperatures during multi-bubble cavitation. *Nature* **401**, 772–775 (1999).
10. S. J. Putterman, K. R. Weninger, Sonoluminescence: How bubbles turn sound into light. *Annu. Rev. Fluid Mech.* **32**, 445–476 (2000).
11. M. P. Brenner, S. Hilgenfeldt, D. Lohse, Single-bubble sonoluminescence. *Rev. Mod. Phys.* **74**, 425–484 (2002).
12. K. S. Suslick, D. J. Flannigan, Inside a collapsing bubble: Sonoluminescence and the conditions during cavitation. *Annu. Rev. Phys. Chem.* **59**, 659–683 (2008).
13. D. J. Flannigan, K. S. Suslick, Inertially confined plasma in an imploding bubble. *Nat. Phys.* **6**, 598–601 (2010).
14. A. A. Kornilova, V. I. Vysotskii, N. N. Sysoev, A. V. Desyatov, Generation of X-rays at bubble cavitation in a fast liquid jet in dielectric channels. *J. Surf. Investig. Synchrotron Neutron Tech.* **3**, 275–283 (2009).
15. D. A. Staack, R. P. Geiger, Processing of dielectric fluids with mobile charge carriers. U.S. Patent US20130161 (2016).
16. L. Wang, Y. Yi, C. Wu, H. Guo, X. Tu, One-step reforming of CO_2 and CH_4 into high-value liquid chemicals and fuels at room temperature by plasma-driven catalysis. *Angew. Chem. Int. Ed.* **56**, 13679–13683 (2017).
17. B. R. Locke, M. Sato, P. Sunka, M. R. Hoffmann, J.-S. Chang, Electrohydraulic discharge and nonthermal plasma for water treatment. *Ind. Eng. Chem. Res.* **45**, 882–905 (2006).
18. D. Staack, A. Fridman, A. Gutsol, Y. Gogotsi, G. Friedman, Nanoscale corona discharge in liquids, enabling nanosecond optical emission spectroscopy. *Angew. Chem. Int. Ed.* **47**, 8020–8024 (2008).
19. J. A. C. Broekaert, Analytical chemistry: Plasma bubbles detect elements. *Nature* **455**, 1185–1186 (2008).
20. D. Mariotti, R. M. Sankaran, Microplasmas for nanomaterials synthesis. *J. Phys. D. Appl. Phys.* **43**, 323001 (2010).
21. G. Fridman, G. Friedman, A. Gutsol, A. B. Shekhter, V. N. Vasilets, A. Fridman, Applied plasma medicine. *Plasma Process. Polym.* **5**, 503–533 (2008).
22. J. Herberholz, B. Schmitz, Flow visualisation and high speed video analysis of water jets in the snapping shrimp (*Alpheus heterochaelis*). *J. Comp. Physiol. A.* **185**, 41–49 (1999).
23. J. Herberholz, B. Schmitz, Role of mechanosensory stimuli in intraspecific agonistic encounters of the snapping shrimp (*Alpheus heterochaelis*). *Biol. Bull.* **195**, 156–167 (1998).
24. G. J. Vermeij, *Nature: An Economic History* (Princeton Univ. Press, 2009).
25. D. Lohse, B. Schmitz, M. Versluis, Snapping shrimp make flashing bubbles. *Nature* **413**, 477–478 (2001).
26. C. Darwin, *On the Origin of Species by Means of Natural Selection, 1859* (Penguin Books, 1968).
27. E. E. Werner, D. J. Hall, Optimal foraging and the size selection of prey by the bluegill sunfish (Lepomis macrochirus). *Ecology* **55**, 1042–1052 (1974).
28. G. A. Parker, J. M. Smith, Optimality theory in evolutionary biology. *Nature* **348**, 27–33 (1990).
29. T. Kaji, A. Anker, C. S. Wirkner, A. R. Palmer, Parallel saltational evolution of ultrafast movements in snapping shrimp claws. *Curr. Biol.* **28**, 106–113.e4 (2018).

30. M. Versluis, B. Schmitz, A. von der Heydt, D. Lohse, How snapping shrimp snap: Through cavitating bubbles. *Science* **289**, 2114–2117 (2000).
31. F. A. Everest, R. W. Young, M. W. Johnson, Acoustical characteristics of noise produced by snapping shrimp. *J. Acoust. Soc. Am.* **20**, 137–142 (1948).
32. J. Herberholz, B. Schmitz, Signaling via water currents in behavioral interactions of snapping shrimp (*Alpheus heterochaelis*). *Biol. Bull.* **201**, 6–16 (2001).
33. J. A. Cook, A. M. Gleeson, R. M. Roberts, R. L. Rogers, A spark-generated bubble model with semi-empirical mass transport. *J. Acoust. Soc. Am.* **101**, 1908–1920 (1997).
34. S. Buogo, G. B. Cannelli, Implosion of an underwater spark-generated bubble and acoustic energy evaluation using the Rayleigh model. *J. Acoust. Soc. Am.* **111**, 2594–2600 (2002).
35. P. Xiao, D. Staack, Microbubble generation by microplasma in water. *J. Phys. D. Appl. Phys.* **47**, 355203 (2014).
36. O. Baghdassarian, B. Tabbert, G. A. Williams, Luminescence characteristics of laser-induced bubbles in water. *Phys. Rev. Lett.* **83**, 2437–2440 (1999).
37. V. Lazic, J. J. Laserna, S. Jovicevic, Insights in the laser-induced breakdown spectroscopy signal generation underwater using dual pulse excitation—Part I: Vapor bubble, shockwaves and plasma. *Spectrochim. Acta Part B At. Spectrosc.* **82**, 42–49 (2013).
38. V. Lazic, J. J. Laserna, S. Jovicevic, Insights in the laser induced breakdown spectroscopy signal generation underwater using dual pulse excitation—Part II: Plasma emission intensity as a function of interpulse delay. *Spectrochim. Acta Part B At. Spectrosc.* **82**, 50–59 (2013).
39. D. Hess, C. Brücker, F. Hegner, A. Balmert, H. Bleckmann, Vortex formation with a snapping shrimp claw. *PLOS ONE* **8**, e77120 (2013).
40. P. Koukouvinis, C. Bruecker, M. Gavaises, Unveiling the physical mechanism behind pistol shrimp cavitation. *Sci. Rep.* **7**, 13994 (2017).
41. S. N. Patek, W. L. Korff, R. L. Caldwell, Biomechanics: Deadly strike mechanism of a mantis shrimp. *Nature* **428**, 819–820 (2004).
42. S. N. Patek, R. L. Caldwell, Extreme impact and cavitation forces of a biological hammer: Strike forces of the peacock mantis shrimp *Odontodactylus scyllarus*. *J. Exp. Biol.* **208**, 3655–3664 (2005).
43. S. N. Patek, B. N. Nowroozi, J. E. Baio, R. L. Caldwell, A. P. Summers, Linkage mechanics and power amplification of the mantis shrimp's strike. *J. Exp. Biol.* **210**, 3677–3688 (2007).
44. S. M. Cox, D. Schmidt, Y. Modarres-Sadeghi, S. N. Patek, A physical model of the extreme mantis shrimp strike: Kinematics and cavitation of Ninjabot. *Bioinspir. Biomim.* **9**, 16014 (2014).
45. A. Anker, S. T. Ahyong, P. Y. Noël, A. R. Palmer, Morphological phylogeny of alpheid shrimps: Parallel preadaptation and the origin of a key morphological innovation, the snapping claw. *Evolution* **60**, 2507–2528 (2006).
46. P. Cignoni, M. Callieri, M. Corsini, M. Dellepiane, F. Ganovelli, G. Ranzuglia, Meshlab: An open-source mesh processing tool, in *Eurographics Italian Chapter Conference*, V. Scarano, R. De Chiara, U. Erra, Eds. (The Eurographics Association, 2008).
47. M. Corsini, P. Cignoni, R. Scopigno, Efficient and flexible sampling with blue noise properties of triangular meshes. *IEEE Trans. Vis. Comput. Graph.* **18**, 914–924 (2012).
48. D. H. Cato, M. J. Bell, *Ultrasonic Ambient Noise in Australian Shallow Waters at Frequencies up to 200 kHz* (DSTO Materials Research Laboratory, 1992), p. No. MRL-TR-91-23.
49. G. S. Settles, *Schlieren and Shadowgraph Techniques: Visualizing Phenomena in Transparent Media* (Springer Science & Business Media, ed. 1, 2012).
50. R. Hiller, K. Weninger, S. J. Putterman, B. P. Barber, Effect of noble gas doping in single-bubble sonoluminescence. *Science* **266**, 248–250 (1994).
51. D. J. Flannigan, K. S. Suslick, Plasma line emission during single-bubble cavitation. *Phys. Rev. Lett.* **95**, 44301 (2005).
52. C.-D. Ohl, Probing luminescence from nonspherical bubble collapse. *Phys. Fluids* **14**, 2700–2708 (2002).
53. O. Supponen, D. Obreschkow, M. Tinguely, P. Kobel, N. Dorsaz, M. Farhat, Scaling laws for jets of single cavitation bubbles. *J. Fluid Mech.* **802**, 263–293 (2016).
54. H. Lamb, *Hydrodynamics* (Cambridge Univ. Press, 1932).
55. P. R. N. Childs, *Rotating Flow* (Elsevier, 2010).
56. S. F. Hoerner, *Fluid-Dynamic Drag: Practical Information on Aerodynamic Drag and Hydrodynamic Resistance* (Hoerner Fluid Dynamics, 1965).
57. D. Obreschkow, P. Kobel, N. Dorsaz, A. de Bosset, C. Nicollier, M. Farhat, Cavitation bubble dynamics inside liquid drops in microgravity. *Phys. Rev. Lett.* **97**, 094502 (2006).
58. M. Tinguely, D. Obreschkow, P. Kobel, N. Dorsaz, A. de Bosset, M. Farhat, Energy partition at the collapse of spherical cavitation bubbles. *Phys. Rev. E Stat. Nonlin. Soft Matter Phys.* **86**, 046315 (2012).
59. B. P. Barber, thesis (1992).
60. W. Lauterborn, H. Bolle, Experimental investigations of cavitation-bubble collapse in the neighbourhood of a solid boundary. *J. Fluid Mech.* **72**, 391–399 (1975).
61. W. Lauterborn, C.-D. Ohl, Cavitation bubble dynamics. *Ultrason. Sonochem.* **4**, 65–75 (1997).
62. I. Akhatov, O. Lindau, A. Topolnikov, R. Mettin, N. Vakhitova, W. Lauterborn, Collapse and rebound of a laser-induced cavitation bubble. *Phys. Fluids* **13**, 2805–2819 (2001).
63. E.-A. Brujan, K. Nahen, P. Schmidt, A. Vogel, Dynamics of laser-induced cavitation bubbles near an elastic boundary. *J. Fluid Mech.* **433**, 251–281 (2001).

Acknowledgments: We appreciate the help from members in Plasma Engineering and Non-equilibrium Processing Laboratory (K. Wang, M. Burnette, N. Gawloski, J. Lassalle, C. Campbell, and B. Swain). **Funding:** This work was supported by the NSF (grant PHY-1057175) and the Robertson-Finley Foundation. **Author contributions:** D.S. conceived the project. X.T. designed and constructed the experimental apparatus, performed experiments, and processed data with ongoing advice from D.S. All authors contributed to data interpretation and manuscript preparation. **Competing interests:** D.S. and X.T. are inventors on a patent currently pending with Texas A&M University related to this work (no. 62/699,841; filed on 18 July 2018). The authors declare that they have no other competing interests. **Data and materials availability:** All data needed to evaluate the conclusions in the paper are present in the paper and/or the Supplementary Materials. Additional data related to this paper may be requested from the authors.

Submitted 13 July 2018
Accepted 30 January 2019
Published 15 March 2019
10.1126/sciadv.aau7765

Citation: X. Tang, D. Staack, Bioinspired mechanical device generates plasma in water via cavitation. *Sci. Adv.* **5**, eaau7765 (2019).